PHYSICAL REVIEW D VOLUME 14, NUMBER 3 1 AUGUST 1976

Measurements of exclusive photoproduction processes at large values of t and u from 4 to 7.5 GeV*

R. L. Anderson, D. B. Gustavson, D. M. Ritson, and G. A. Weitsch[†]
Stanford Linear Accelerator Center, Stanford University, Stanford, California 94305

H. J. Halpern,[‡] R. Prepost, D. H. Tompkins,[§] and D. E. Wiser
University of Wisconsin, Madison, Wisconsin 53706
(Received 2 February 1976)

Exclusive photoproduction cross sections have been measured for the processes $\gamma p \to \pi^+ n$, $\gamma p \to \pi^0 p$, $\gamma p \to \pi^- \Delta^{++}$, $\gamma p \to \rho^0 p$, $\gamma p \to K^+ \Lambda$, and $\gamma p \to K^+ \Sigma^0$ at large t and u values at several energies for each process between 4 and 7.5 GeV. These measurements taken together with past data taken at small values of t and u provide complete angular distributions. The data show the usual small t and u peaks and a central region in which the cross section decreases approximately as s^{-7}. The results are discussed within the context of parton or constituent models.

I. INTRODUCTION

This paper presents angular distributions for exclusive photoproduction processes at large values of t and u measured with a missing-mass spectrometer technique at the Stanford Linear Accelerator Center (SLAC). These data, taken together with previous data at values of t from 0 to -2 $(\mathrm{GeV}/c)^2$ and small values of u from 0 to -1 $(\mathrm{GeV}/c)^2$, provide complete angular distributions for several exclusive photoproduction processes at photon energies in the range from 4 to 7.5 GeV. The exclusive channels for which measurements have been made in this experiment are listed in Table I.

The results for the process $\gamma p \to \pi^+ n$ have been published in preliminary form.[1] Prior to this set of measurements, data existed over a limited region of the forward t channel and the backward u channel. Cross sections at large t and u values are much smaller than cross sections for the extreme forward and backward regions and consequently are difficult to measure. The data of Ref. 1 showed that the forward and backward regions are quite distinct from the region of large c.m. angles in that the large-c.m.-angle cross sections at fixed angle are characterized by a fairly steep energy dependence (approximately s^{-7}). This "central region" for a variety of exclusive processes is the focus of the present measurements.

The large-c.m.-angle region is currently a very active area of study, both experimentally and theoretically. The inclusive or inelastic hadron processes at large transverse momentum have been observed to show a transverse-momentum behavior considerably in excess of the $e^{-6p_\perp}$ predicted on the basis of thermodynamic models, and exclusive scattering processes have been observed to show a simple power-law energy dependence at fixed c.m. angle. These features have generated considerable theoretical thought, focusing primarily on parton or constituent models. The exclusive processes reported in this paper will be examined from the standpoint of these constituent models to determine if any simple scaling features at large c.m. angles emerge.

Exclusive processes in Regge-type theories are expected to factorize in the form $d\sigma/dt \sim f_1(t) s^{f_2(t)}$ for t-channel behavior and $d\sigma/du \sim g_1(u) s^{g_2(u)}$ for u-channel behavior. This behavior has been confirmed for the small t and u regions, but is not expected to deal adequately with the large t and u region. Models which deal with this region are the constituent or parton models, of which a comprehensive summary may be found in the review paper of Sivers, Brodsky, and Blankenbecler.[2] Constituent models of the type of Gunion, Brodsky, and Blankenbecler,[3] and Landshoff and Polkinghorne,[4] while not scale invariant, nevertheless show a scaling behavior. These constituent models, in general, predict cross sections for the large t and u region to be of the

TABLE I. List of reactions and photon energies covered in this experiment.

Process	Energy (GeV)
$\gamma p \to \pi^+ n$	4, 5, 7.5
$\gamma p \to \pi^0 p$	4, 5
$\gamma p \to \pi^- \Delta^{++}$	4, 5
$\gamma p \to \rho^0 p$	4, 6
$\gamma p \to K^+ \Lambda$	4, 6
$\gamma p \to K^+ \Sigma^0$	4, 6

form

$$\frac{d\sigma}{dt} \sim \frac{1}{s^N} f(\cos\theta^*) ,$$

where θ^* is the c.m. scattering angle.

The constituent-interchange model of Brodsky, Blankenbecler, and Gunion[5] makes specific predictions for the power dependence of s and the functional dependence of $f(\cos\theta^*)$, but does not predict absolute cross-section values. General dimensional counting arguments of the type of Matveev, Muradyan, and Tavkhelidze,[6] and Brodsky and Farrar[7] also make specific predictions for the s dependence of exclusive processes. Specifically, the s-power fixed-angle behavior for exclusive processes is expected to be

$$\frac{d\sigma}{dt} \sim \frac{1}{s^{N-2}} f(\cos\theta^*) ,$$

where N is the number of "elementary" fields participating in the reaction. If the photon is assumed to be one elementary field, then the prediction for meson photoproduction is

$$\frac{d\sigma}{dt} \sim \frac{1}{s^7} f(\cos\theta^*) .$$

It will be shown that the results of the present experiment are consistent with these predictions in the large-c.m.-angle region.

Both Regge and constituent models also closely connect the exclusive and inclusive cross sections. The connection is prescribed for any theory; the correspondence principle of Bjorken and Kogut[8] is the connection for constituent-type theories. In a subsequent paper, we will report the results of inclusive photoproduction of π, K, and p in the energy range 5–20 GeV, and discuss the quantitative connection between the exclusive and inclusive domains.

An additional area of interest is large-angle proton Compton scattering. Constituent models of the above types will apply to this process and similar predictions can be made. However, this process can be treated more specifically, since $\gamma p \rightarrow \gamma p$ in a constituent model is simply the elastic scattering of photons from the constituents, and an absolute cross section in terms of the Klein-Nishina expression, constituent charges, and the proton form factor can be derived. Previous results on inelastic Compton scattering and large-angle muon-pair production suggest cross sections considerably higher than the constituent-model predictions. While the large-angle exclusive Compton-scattering cross section has not been measured directly in this experiment, the exclusive large-angle photoproduction of ρ mesons has been measured and can be used to set a lower limit on the Compton-scattering cross section by using the vector-dominance contribution to the cross section through the relation

$$\frac{d\sigma}{dt}(\gamma p \rightarrow \gamma p) = \frac{\alpha}{4}\left(\frac{\gamma_\rho^2}{4\pi}\right)^{-1} \frac{d\sigma}{dt}(\gamma p \rightarrow \rho^0 p)_{\text{trans}} .$$

The comparison to a constituent-model prediction is made in the last section.

II. EXPERIMENT AND APPARATUS

This experiment was performed at SLAC using the 8-GeV/c spectrometer facility in End Station A. Figure 1 shows the beam setup. The detailed aspects of the experiment are discussed below.

A. Beam preparation and monitoring

Where lower photon intensities were sufficient, a pure bremsstrahlung beam was prepared with a radiator 52 m upstream from the liquid hydrogen target (distant targeting) followed by a well-shielded dump magnet to remove the main electron beam. In order to obtain maximum photon beam intensities, a radiator was inserted 2 m upstream of the hydrogen target (near targeting) and both electrons and photons passed through the hydrogen target.

The distant-targeted pure photon beam was collimated to a spot size of approximately 1 cm by 1 cm at the target by a high-power water-cooled collimator about one-third of the distance between the radiator and the hydrogen target. A secondary collimator, located two-thirds of the distance between radiator and target, intercepted any halo surrounding the beam after primary collimation. The charged-particle spray remaining after this collimation was removed by a second sweep magnet and intercepted by a lead brick wall, which contained a collimator of fixed size to pass the main photon beam. To keep backgrounds down after passing through the hydrogen target, the beam went through a 54-m-long helium duct. The beam was stopped and monitored in a secondary-emission quantameter (SEQ) located in a well-shielded cave just inside the end station. The secondary-emission quantameter was a secondary standard and was periodically calibrated rela-

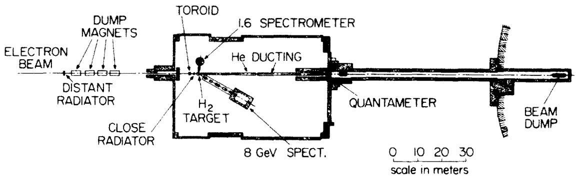

FIG. 1. Plan view of experimental layout.

tive to a silver calorimeter that served as the primary standard.[9] A beam intensity of 5×10^{11} equivalent quanta (EQ) per second was typically obtained.

For the near-targeting operating mode, remotely controlled radiators of various thickness were inserted just before the target, the SEQ was lowered out of the beam line, and the primary electrons plus the radiator-produced photon beam were deposited in the high-power water-cooled beam dump (Beam Dump East) buried in a hill 91 m behind the end station. The helium duct beyond the target significantly reduced backgrounds by reducing the material with which the electron beam could interact.

B. Targets

The hydrogen target cells were aluminum cylinders 8.89 cm in diameter with 0.025-cm-thick walls and 0.010-cm-thick aluminum end caps. The target-cell lengths were 15.2 and 30.6 cm, and identical dummy cells were used to measure empty-target backgrounds. The liquid hydrogen was circulated through the cells and to a heat exchanger by a pump in order to eliminate any variations of density induced by heating due to the electron beam.

C. Particle identification

The counting system is shown in Fig. 2. The system was designed to simultaneously identify pions, kaons, and protons over the full range of spectrometer momenta. In addition to trigger counters and hodoscope systems to measure angles and momenta, the system contained three threshold Čerenkov counters and a time-of-flight system which could be used in various configurations to give simultaneous particle identification over the full range of the experiment. The three threshold Čerenkov counters consisted of a Lucite counter, a Freon-12 counter operating up to 5 atm, and a Freon-13 counter operating up to 19 atm. The Lucite counter was used to discriminate against protons below 1.5 GeV/c and nonrelativistic background particles. The Freon-12 counter was set to count pions only. At full pressure, the Freon-13 counter thresholds for pions, kaons, and protons were 0.77, 2.75, and 5.2 GeV/c, respectively. In addition, a time-of-flight system could be used to identify kaons with momenta below 2.75 GeV/c, and protons with momenta below 5.5 GeV/c. To measure times of flight, the primary electron beam was modulated into 0.5-nsec-wide bursts, occurring at 25-nsec intervals. The spectrometer counting system measured the relative arrival times of the detected particles at the scintillation counter S-2, which was 22.86 m from the hydrogen target. The time resolution obtained in this experiment was 1 nsec full width at half maximum. The time-of-flight system was only used when necessary, as the required modulation of the primary electron beam resulted in a substantial reduction in beam intensity.

Pions below 1.4 GeV/c were identified by using the Lucite counter, and for momenta above 1.4 GeV/c the two gas Čerenkov counters were used. Protons were identified with a "default" trigger by placing the Lucite counter in veto at low momentum, and at least one gas Čerenkov counter in veto at higher momenta. For kaons with momenta below 2.75 GeV/c, time of flight gave excellent discrimination between protons and kaons. A "missing mass" technique looking for a kinematic step at the appropriate missing mass was used to analyze the particle yields. Since unwanted particles appear as a monotonic background underneath the step, only moderate rejection of unwanted particles was required. This monotonic background was small for all the measurements.

D. Spectrometer hodoscope systems and focusing properties

To first order, the focusing of the 8-GeV spectrometer was parallel to point for the production angle in the horizontal plane, and point to point for the momentum in the vertical plane.[10] The production-angle focal plane was perpendicular to the central ray and separated from the momentum focal plane (P coordinate) by 0.5 m. Two hodoscopes placed at each of the respective focal planes allowed separate measurements of production angle (θ hodoscope) and momentum (P hodoscope). Additionally, a 21-unit "X hodoscope" was installed 2 m in front of the θ hodoscope. In conjunction with the θ hodoscope, it permitted the reconstruction of the interaction point in the target. The solid-angle acceptance was determined for the vertical plane by variable entrance slits, and for the horizontal production plane by the scintillation counters at the θ focus.

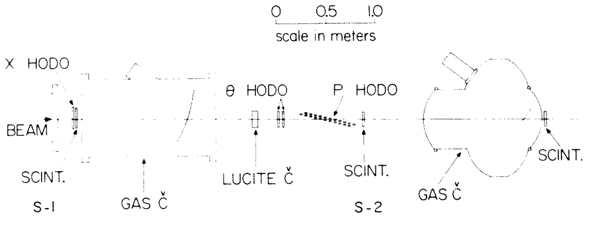

FIG. 2. 8-GeV spectrometer-counter layout.

E. Event processing

An event satisfying the appropriate combination of scintillation and Čerenkov counters triggered the fast electronics and initiated an interrogation strobe for the hodoscope elements. The information from the hodoscope elements was stored in buffers, arranged as one buffer bit per hodoscope scintillator. The strobe pulse was 5 nsec in width and only one such event could be stored per accelerator spill (1.5 μsec). Photon-beam intensities were adjusted such that the computer dead-time effects were always less than 15% (typically 5%). Rate effects in the fast electronics were kept to less than 5%. These dead-time effects were well understood and the data were corrected accordingly.

The on-line computer (SDS-9300) decoded the hodoscope-bit patterns during the time interval between accelerator pulses with the following criteria for event selection.

(1) A single "good" event pattern in each of the three hodoscopes (X, θ, and P) was required for unambiguous event identification. For the X hodoscope with nonoverlapping elements, a good event pattern required counts in a single counter or two adjacent counters. For the θ and P hodoscopes, which were constructed of two overlapping rows of scintillators, counts in one to three adjacent elements represented an acceptable event.

(2) In the θ and P hodoscopes, the particle was required to be within a fiducial region restricted to a well-understood region of the spectrometer acceptance. This fiducial region was symmetric about the central spectrometer ray, and corresponded to a momentum acceptance of $\Delta P/P = 3.76\%$ in 18 bins of 0.209% each, and a θ acceptance $\Delta\theta$ of 10 mrad in 33 bins of 0.302 mrad each. The vertical acceptance, $\Delta\phi$, was set typically to 24 mrad by adjustable slits at the spectrometer entrance.

(3) The event was required to originate from the vicinity of the target. This cut was made by reconstructing the particle trajectory from the coordinates determined at the X and θ hodoscopes. The spatial resolution was of the order of one target length, sufficient to achieve substantial rejection of unwanted background particles penetrating the shielding. A few percent of true events were rejected by this cut.

When the time-of-flight system was used, the events passing the hodoscope and target cuts were subjected to a software time cut applied to the output of a time-to-pulse-height converter (THC). A single channel in the THC corresponded to a time resolution of 0.37 nsec.

Events which satisfied the above conditions were within the well-understood acceptance of the spectrometer and had a precisely determined momentum and a precisely determined production angle. The particle identity had previously been determined by the combination of Čerenkov counters in the trigger, and that information was passed to the computer through special flag bits set by the fast electronics. The missing mass associated with the particle was then calculated, and the event was entered into the corresponding missing-mass histogram for that particular type. Displays for these histograms, as well as those for monitoring hodoscope and THC performance, were readily available during data taking.

F. Data taking

Data were taken over a range of missing masses about the kinematic threshold. The missing mass was more efficiently stepped by changing the spectrometer momentum rather than changing the spectrometer angle. Thus, to determine a cross section, the spectrometer angle was fixed and the spectrometer momentum was stepped to make a set of runs. The duration of an individual run was typically 5 to 20 minutes. At the end of an individual run, the counts per missing-mass bin were normalized to the number of equivalent quanta (EQ) measured by the beam monitor, and the result was stored on an external magnetic drum of the computer. The computer software combined the set of runs taken at a fixed specified spectrometer angle into a missing-mass "sweep." In order to eliminate systematic errors, the data for a sweep were accumulated in interleaved order.

The final data from a running period therefore consisted of a series of missing-mass sweeps which were subsequently analyzed off-line in order to determine the size of the kinematic steps and ultimately the cross sections.

G. Data analysis

The cross sections were obtained from an analysis of bremsstrahlung yield curves where the angle and momentum of the detected particle are determined by a spectrometer.[14] For a two-body process such as $\gamma p \to \pi^+ n$, the angle and momentum determinations of the π^+ meson determine the energy of the photon which initiated the reaction. As the threshold for the process is crossed by changing the angle or the momentum of the spectrometer, a step rather than a peak is seen in the yield curve since the bremsstrahlung spectrum is continuous up to the end-point energy. The size and shape of the step reflects the magnitude of the cross section at the step and the shape of the end point of the bremsstrahlung spectrum. The step occurs, of course, at a missing mass corresponding to the recoiling particle. As the yield curve is continued to larger missing-mass values and other processes become kinematically possible, additional steps will appear in the yield curve at the appropriate value of the missing mass.

Thus the detection of the reaction $\gamma p \rightarrow \pi^+ n$ corresponds to a step in the detected pion yield measured as a function of π^+ momentum for a fixed angle and a fixed bremsstrahlung end-point energy. The step appears at a missing mass corresponding to that of the undetected recoil neutron, while for the process $\gamma p \rightarrow \pi^- \Delta^{++}$ the missing mass corresponds to the mass of the Δ^{++} resonance. Similarly, for the reactions $\gamma p \rightarrow \pi^0 p$ and $\gamma p \rightarrow \rho^0 p$ the recoil proton is detected, and the steps in the proton yield correspond to the π^0 mass and ρ^0 mass, respectively. For the processes $\gamma p \rightarrow K^+ \Lambda$ and $\gamma p \rightarrow K^+ \Sigma^0$, the K^+ mesons are detected, and the missing-mass steps in the yield curves correspond to the Λ and Σ^0 masses, respectively.

Figure 3 shows typical yield curves for each of the processes studied in this experiment. The figures show the typical kinematic step at the threshold for producing the appropriate particle at fixed momentum and angle. Each cross-section measurement corresponds to a separate yield curve except for the processes $\gamma p \rightarrow K^+ \Lambda$ and $\gamma p \rightarrow K^+ \Sigma^0$, where the thresholds are kinematically very close. The yield curves are analyzed by fitting them with a smoothly varying background function plus a function with the appropriate shape for the kinematic step. The figure shows the background function plus the kinematic step function as solid lines. The ordinate is proportional to the yield per EQ, and the abscissa represents the missing mass squared in $(\mathrm{GeV}/c^2)^2$. In each case the threshold step is clearly visible. The kinematic function with the appropriate shape for the kinematic step consisted of the following components:

(1) the bremsstrahlung spectrum,

(2) the Jacobian, $J(k, t \mid P, \theta)$ for the reaction being fitted, where k is the effective photon energy, t is the 4-momentum-transfer squared, P is the momentum for a missing-mass bin, and θ is the particle production angle,

(3) a linear approximation to the k and t dependences of the cross section as the values for these variables varied over the range of missing mass used in a fit to the kinematic step;

(4) a Gaussian smearing term to include the spectrometer resolution function.

In addition, for the cases of Δ and ρ production, the expression for the shape of the kinematic step was folded with the appropriate Breit-Wigner mass spectrum. A standard fitting procedure was then used to determine the best values of the coefficients for the sizes of the kinematic-step and background terms. The separation of the background from the signal depended to some extent on the assumptions made as to the functional dependence of the background. The background subtraction was assigned an uncertainty of 25% to take into account this dependence on the analysis assumptions. This error assignment was believed to be conservative.

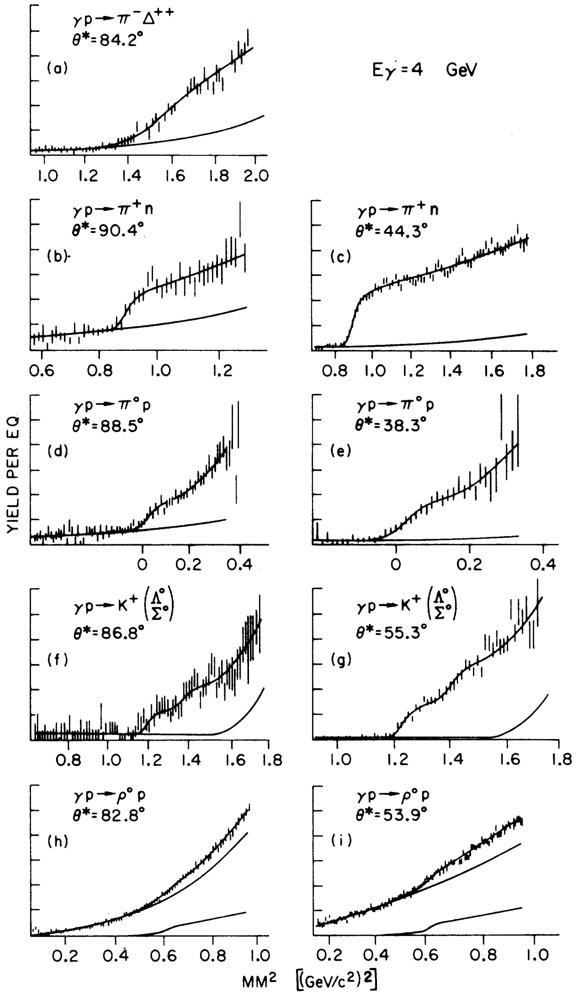

FIG. 3. Typical missing-mass sweeps at $E_\gamma = 4.0$ GeV for the processes measured in this experiment, showing (a) $\gamma p \rightarrow \pi^- \Delta^{++}$, (b) and (c) $\gamma p \rightarrow \pi^+ n$, (d) and (e) $\gamma p \rightarrow \pi^0 p$, (f) and (g) $\gamma p \rightarrow K^+ (\Lambda/\Sigma^0)$, and (h) and (i) $\gamma p \rightarrow (\rho^0 + \omega) p$. The solid lines show the best fits to the data assuming the functional forms for signal and background discussed in the text. The meson c.m. angle θ^* is indicated for each figure. (h) and (i) also show the subtracted signal as a separate solid line.

To obtain absolute cross sections, the following set of corrections was made:

(1) The θ and momentum hodoscopes, consisting of overlapping arrays of scintillation counters, were 99% efficient, while the X hodoscope (a single row) was 98% efficient. The overall efficiency of the hodoscopes was $(96\pm2)\%$.

(2) Electron knockons in the material of the detection array caused ambiguities in one or more hodoscopes, resulting in "good" events being rejected by the on-line software. This loss through knock-on events was $(7\pm3)\%$.

(3) Particles were removed by interactions in the material of the counter array. This loss was $(16\pm3)\%$.

(4) For spectrometer angles less than 64° the full target length was seen by the spectrometer, while at larger angles a small effective-target-length correction was made.

(5) The loss of particles by absorption in the target was between 1% and 2%.

(6) The efficiencies of the gas Čerenkov counters were typically 97%, and the Lucite-counter efficiency was 95%.

(7) Rate-dependent losses in the fast electronics were always less than 5%.

(8) For pions and kaons, a correction was made for the losses by decay in the 22.8-m flight path through the spectrometer.

The data were normalized using the absolute beam intensity calibration and the known solid-angle acceptance of the spectrometer. As a check, electron-proton elastic cross sections were measured and agreed with the known cross sections to 5%.

The systematic errors (in addition to those discussed in the fitting procedure) were estimated to be 7%. These errors came chiefly from the solid-angle calibration and the uncertainties associated with the absorption corrections and detection efficiencies of the particles.

III. RESULTS

The results of these measurements are tabulated in Tables 2-6 and shown in Figs. 4-18. The cross sections $d\sigma/dt$ are shown plotted both as a function of t and $\cos\theta^*$, where θ^* is the c.m. scattering angle. The cross sections are also plotted as $s^7 d\sigma/dt$ versus $\cos\theta^*$ on a common plot for each exclusive process in order to show the features of the fixed-angle energy dependence relative to the s^{-7} behavior expected on the basis of the large-angle scattering models.

A. The reaction $\gamma p\to\pi^+ n$

Figures 4-6 and Table II present the data for the process $\gamma p\to\pi^+ n$ at 4, 5, and 7.5 GeV, a preliminary report of which may be found in Ref. 1. The errors were calculated by adding, in quadrature, the statistical errors, systematic errors, and the error introduced by the subtraction of the background underneath the kinematic step. A detailed discussion of the errors is found in of Sec. II(G).

For $|t|$ values up to about 2 $(\mathrm{GeV}/c)^2$, the data show the typical exponential $(e^{3.3t})$ falloff of the cross section observed by Boyarski *et al.*[11] The

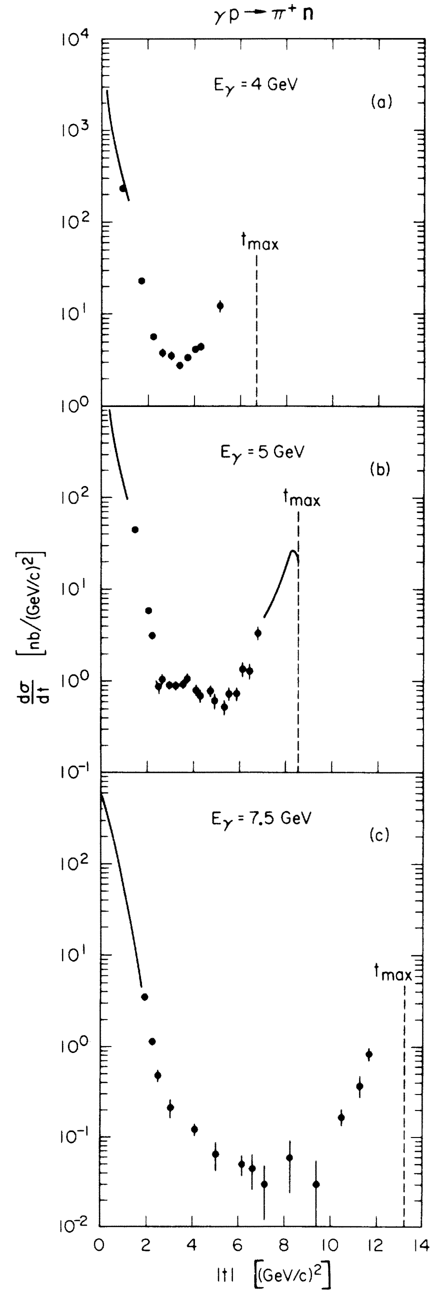

FIG. 4. $d\sigma/dt$ versus t for the reaction $\gamma p\to\pi^+ n$ at (a) $E_\gamma=4.0$ GeV, (b) $E_\gamma=5.0$ GeV, and (c) $E_\gamma=7.5$ GeV.

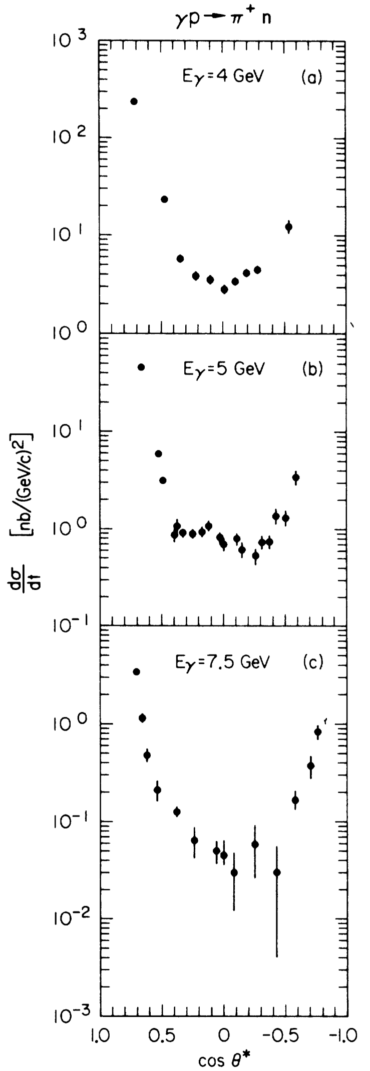

FIG. 5. $d\sigma/dt$ versus $\cos\theta^*$ for the reaction $\gamma p \to \pi^+ n$ at (a) $E_\gamma = 4.0$ GeV, (b) $E_\gamma = 5.0$ GeV, and (c) $E_\gamma = 7.5$ GeV.

data for small $|u|$ values show a slower falloff with u ($e^{1.3u}$), which is in reasonable agreement with the results of Anderson *et al.*[12] The central plateau region is distinct from either of these regions and has only a small dependence on the t or u values, but has a very strong s dependence. The data of Ref. 11 and 12 are indicated on Fig. 4 by the solid lines.

The s dependence of $d\sigma/dt$ at ~90° c.m. is $s^{-7.3\pm.4}$, while examination of Fig. 6 shows that an s^{-7} behavior of $d\sigma/dt$ at a fixed angle represents the data over a wide range of angles.

B. The reaction $\gamma p \to \pi^0 p$

Figures 7–9 and Table III present results for the process $\gamma p \to \pi^0 p$ at 4.0 and 5.0 GeV. Compton

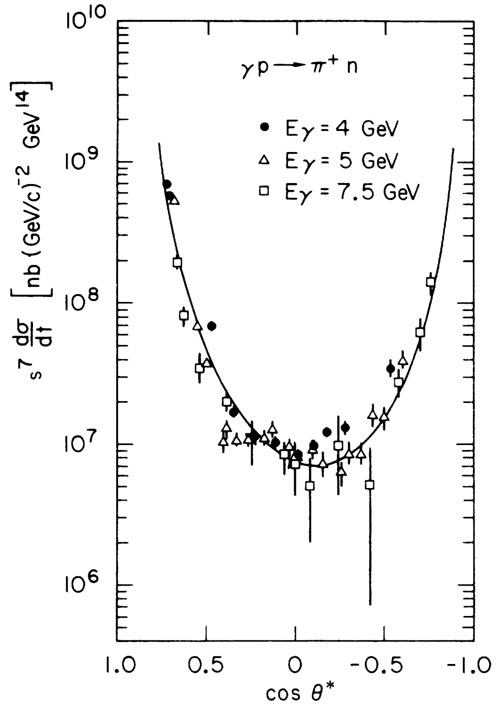

FIG. 6. $s^7 d\sigma/dt$ versus $\cos\theta^*$ for the reaction $\gamma p \to \pi^+ n$. The solid line shows the empirical function $(1-z)^{-5}(1+z)^{-4}$ where ($z = \cos\theta^*$), which is an empirical fit to the angular distribution.

scattering $\gamma p \to \gamma p$ is not distinguishable from the process $\gamma p \to \pi^0 p$ within the resolution of this experiment. On the basis of vector-dominance arguments, the cross section for Compton scattering is expected to be approximately 1/200 that of ρ production. As will be subsequently shown, the ratio of ρ production to π^0 production has been determined in this experiment to be approximately 4 over the region of the π^0 measurements. Consequently, the contribution to the π^0 signal from proton Compton scattering amounts to only a few percent and has accordingly been neglected. Previous data at small t values are indicated in the figures by a solid line.[13,14] The results are very similar to the π^+ data, but the 4.0-GeV π^0 angular distribution gives a dip structure at $|t|$ values of about 2.5 $(\text{GeV}/c)^2$ and 4.5 $(\text{GeV}/c)^2$. Points run at similar kinematic conditions have almost identical systematic errors and therefore this dip structure appears statistically quite significant. This effect is also present but less pronounced in the 5-GeV data at a $|t|$ value of 6.5 $(\text{GeV}/c)^2$. The low-t region again has a characteristic e^{3t} behavior, as may be seen from Fig. 7. The very low t cross sections show a dip structure which is not covered by the data of the present experiment, but which is represented by the solid line in Fig. 7 and

TABLE II. Cross-section tabulation for the process $\gamma p \rightarrow \pi^+ n$.

$-t$ [(GeV/c)^2]	cosθ^*	$d\sigma/dt$ [nb/(GeV/c)^2]
	k = 4 GeV	
0.95	0.716	236 ± 6
1.78	0.468	23.2 ± 1.5
2.21	0.340	5.75 ± 0.52
2.62	0.217	3.85 ± 0.38
3.01	0.101	3.52 ± 0.32
3.37	−0.007	2.84 ± 0.30
3.71	−0.109	3.39 ± 0.24
4.01	−0.198	4.17 ± 0.33
4.29	−0.282	4.47 ± 0.45
5.14	−0.536	12.2 ± 1.9
	k = 5 GeV	
1.44	0.663	44.3 ± 2.4
2.03	0.525	5.81 ± 0.35
2.20	0.486	3.14 ± 0.23
2.54	0.406	0.86 ± 0.14
2.63	0.385	1.07 ± 0.16
2.88	0.327	0.90 ± 0.09
3.21	0.249	0.89 ± 0.10
3.53	0.175	0.92 ± 0.10
3.76	0.121	1.07 ± 0.13
4.13	0.034	0.80 ± 0.11
4.27	0.002	0.69 ± 0.11
4.74	−0.108	0.78 ± 0.11
4.92	−0.150	0.61 ± 0.12
5.37	−0.256	0.52 ± 0.10
5.58	−0.305	0.73 ± 0.12
5.86	−0.370	0.73 ± 0.12
6.12	−0.431	1.35 ± 0.25
6.42	−0.501	1.28 ± 0.25
6.80	−0.590	3.35 ± 0.56
	k = 7.5 GeV	
1.95	0.705	3.45 ± 0.16
2.24	0.661	1.15 ± 0.12
2.54	0.616	0.481 ± 0.079
3.02	0.543	0.212 ± 0.051
4.12	0.377	0.121 ± 0.019
5.04	0.238	0.065 ± 0.023
6.17	0.067	0.050 ± 0.013
6.61	0.000	0.045 ± 0.019
7.17	−0.085	0.030 ± 0.018
8.23	−0.245	0.059 ± 0.033
9.40	−0.422	0.030 ± 0.026
10.43	−0.578	0.169 ± 0.038
11.26	−0.703	0.374 ± 0.097
11.63	−0.759	0.83 ± 0.14

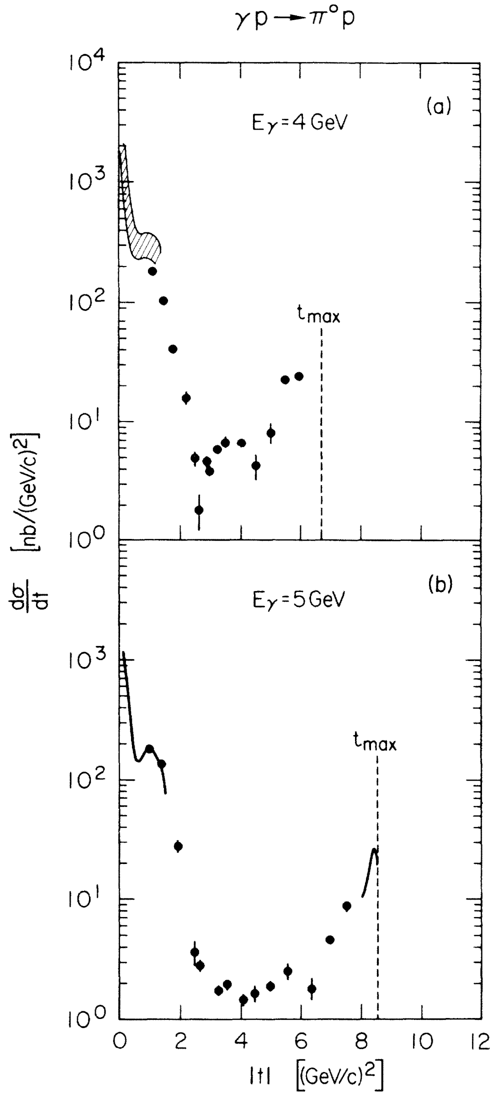

FIG. 7. $d\sigma/dt$ versus t for the reaction $\gamma p \rightarrow \pi^0 p$ at (a) $E_\gamma = 4.0$ GeV and (b) $E_\gamma = 5.0$ GeV.

represents the experiment of Braunschweig *et al.*[13] Data in this energy range for very small u values show a backward peak which reaches a maximum near $u = 0$ and decreases for positive u. The cross section falls rapidly out to $u = -0.4$ (GeV/c)^2, and then continues slowly downward with a characteristic $e^{1.5u}$ behavior. The s dependence of the cross section at fixed u is fairly well represented by s^{-3} at least out to $u = -1.0$(GeV/c)^2. The cross sections again have a central region where the s dependence is much steeper than the forward or backward regions. The s dependence of $d\sigma/dt$ measured at 90° c.m. goes as $s^{-7.6\pm0.7}$. Figure 9 shows that an s^{-7} behavior of $d\sigma/dt$ at fixed angle is a fairly good representation of the data, but the presence of dip structure makes this comparison qualitative in nature. A comparison of the central region values of $d\sigma/dt$ for the $\pi^0 p$ and $\pi^+ n$ data at 4 and 5 GeV shows that the cross sections are similar but that the $\pi^0 p$ cross sections are higher by a factor of approximately 2.

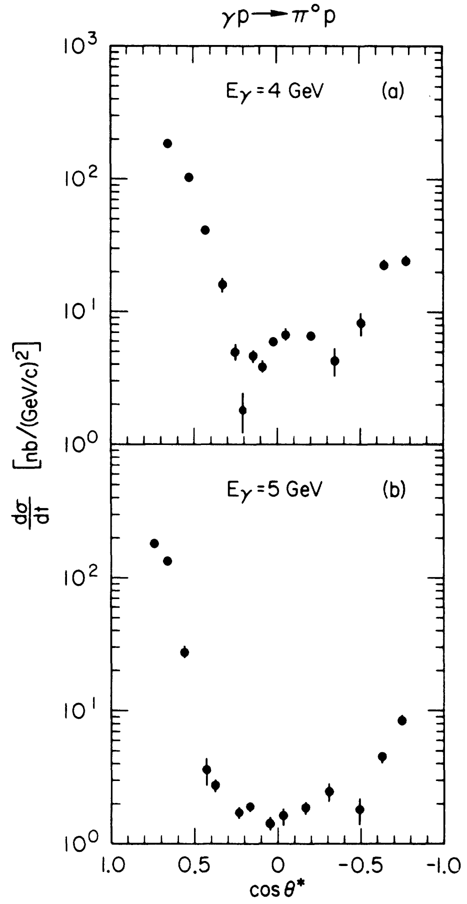

FIG. 8. $d\sigma/dt$ versus $\cos\theta^*$ for the reaction $\gamma p \rightarrow \pi^0 p$ at (a) $E_\gamma = 4.0$ GeV and (b) $E_\gamma = 5.0$ GeV.

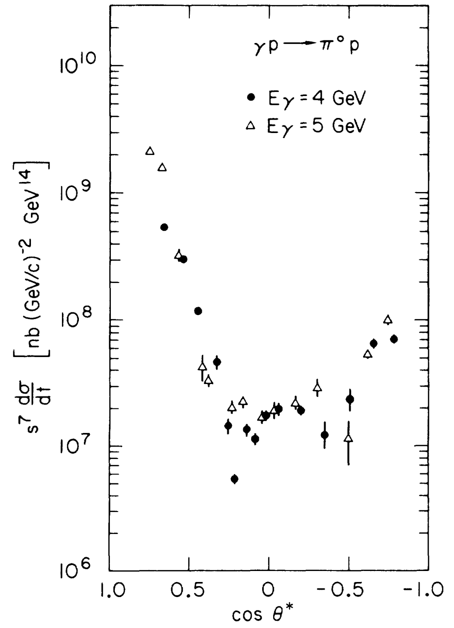

FIG. 9. $s^7 d\sigma/dt$ versus $\cos\theta^*$ for the reaction $\gamma p \rightarrow \pi^0 p$.

TABLE III. Cross-section tabulation for the process $\gamma p \rightarrow \pi^0 p$.

$-t$ [(GeV/c)^2]	$\cos\theta^*$	$d\sigma/dt$ [nb/(GeV/c)^2]
	$k=4$ GeV	
1.19	0.644	184.2 ± 7.9
1.58	0.529	102.9 ± 3.3
1.89	0.435	40.1 ± 2.1
2.24	0.329	15.9 ± 2.0
2.49	0.255	4.93 ± 0.71
2.64	0.211	1.83 ± 0.62
2.88	0.140	4.62 ± 0.51
3.07	0.084	3.87 ± 0.41
3.26	0.025	5.97 ± 0.43
3.53	−0.055	6.78 ± 0.77
4.03	−0.203	6.57 ± 0.48
4.54	−0.356	4.25 ± 1.04
5.05	−0.508	8.06 ± 1.63
5.54	−0.654	22.5 ± 2.0
5.98	−0.785	24.1 ± 2.0
	$k=5$ GeV	
1.10	0.743	179.6 ± 9.5
1.41	0.671	132.6 ± 7.0
1.87	0.562	27.5 ± 3.1
2.44	0.431	3.56 ± 0.84
2.63	0.386	2.78 ± 0.31
3.26	0.238	1.71 ± 0.18
3.57	0.166	1.91 ± 0.16
4.07	0.048	1.42 ± 0.17
4.43	−0.035	1.61 ± 0.24
4.99	−0.167	1.87 ± 0.19
5.58	−0.304	2.45 ± 0.38
6.38	−0.490	1.78 ± 0.37
6.96	−0.626	4.46 ± 0.37
7.49	−0.751	8.40 ± 0.78

C. The reaction $\gamma p \rightarrow \pi^- \Delta^{++}$

Figures 10–12 and Table IV show the results for the process $\gamma p \rightarrow \pi^- \Delta^{++}$ at 4 and 5 GeV. Again, the angular distribution is similar to the π^+ and π^0 data in that the forward and backward peaks are joined by a central region with a steep s dependence (however, with no discernible structure), which goes as $s^{-8.6 \pm 0.8}$ at 90° c.m.. Another significant feature of the π^- data is that the central-region cross sections at fixed energy are approximately 6–7 times larger than the corresponding π^+ values. The small u value peak, while present, is less pronounced than for π^+ production because of the large plateau cross section. The data of Ref. 15 and 16 are indicated by the solid lines in Fig. 10.

D. The reactions $\gamma p \rightarrow K^+ \Lambda$ and $\gamma p \rightarrow K^+ \Sigma^0$

The results for the processes $\gamma p \rightarrow K^+ \Lambda$ and $\gamma p \rightarrow K^+ \Sigma^0$ at 4.0 and 6.0 GeV are presented in Figs. 13–15 and Table V. Although the statistics

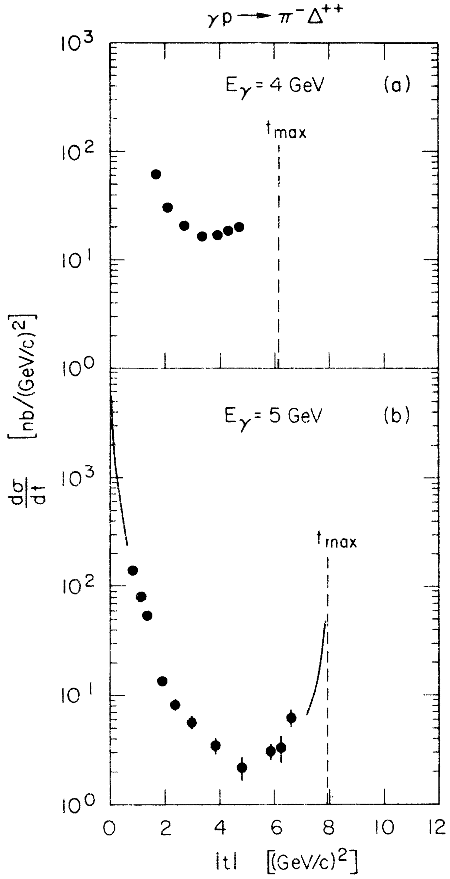

FIG. 10. $d\sigma/dt$ versus t for the reaction $\gamma p \to \pi^-\Delta^{++}$ at (a) $E_\gamma = 4.0$ GeV and (b) $E_\gamma = 5.0$ GeV.

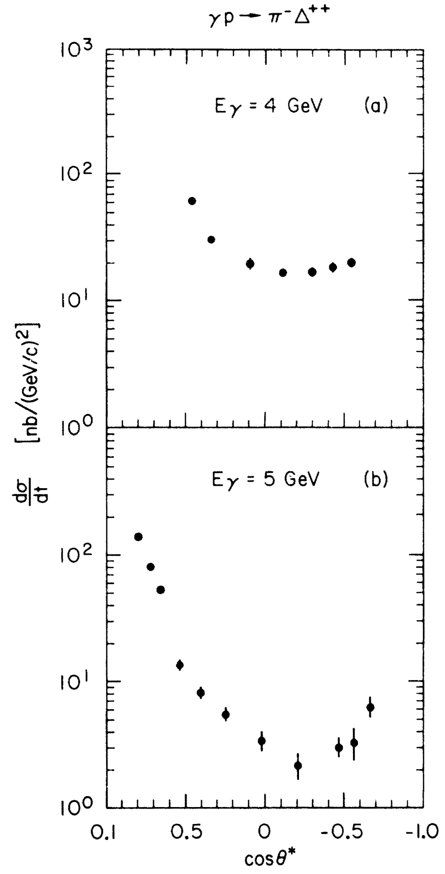

FIG. 11. $d\sigma/dt$ versus $\cos\theta^*$ for the reaction $\gamma p \to \pi^-\Delta^{++}$ at (a) $E_\gamma = 4.0$ GeV and (b) $E_\gamma = 5.0$ GeV.

are lower, the background is small compared with the signal, and no ambiguity is introduced by the assumptions for the shape of the background. The central region shows similar features to those observed for the other processes. The 5-GeV SLAC data taken from Ref. 17 are shown in Figs. 13(a) and 13(c), using an s^{-2} energy dependence to extrapolate to 4 GeV. The small u value data from Ref. 18 are also indicated in Figs. 13(a) and 13(c). The Σ^0/Λ ratio of the present data is consistent with unity, as is the case for the low t value data of Ref. 17. The small u value data of Ref. 18, however, give $\Sigma^0/\Lambda = 1.7 \pm 0.15$ over the u range $-0.7 \leq u \leq -0.2$ $(\mathrm{GeV}/c)^2$.

E. The reaction $\gamma p \to (\rho^0 + \omega)p$

Figures 16–18 and Table VI show the results for ρ plus ω photoproduction at 4.0 and 6.0 GeV. The resolution is not sufficient to separate ρ mesons from ω mesons with the missing-mass technique of this experiment; however, limits can be obtained from the fits to the yield curves, and put ω pro-

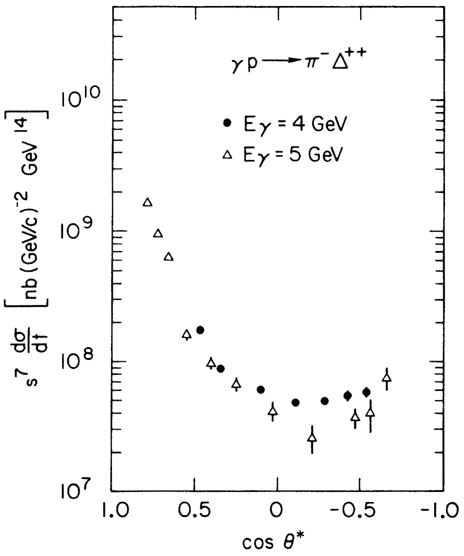

FIG. 12. $s^7 d\sigma/dt$ versus $\cos\theta^*$ for the reaction $\gamma p \to \pi^-\Delta^{++}$.

TABLE IV. Cross-section tabulation for the process $\gamma p \to \pi^- \Delta^{++}$.

$-t$ [(GeV/c)^2]	$\cos\theta^*$	$d\sigma/dt$ [nb/(GeV/c)^2]
	$k = 4$ GeV	
1.63	0.467	61.5 ± 3.0
2.02	0.340	30.5 ± 2.2
2.75	0.100	20.6 ± 0.83
3.39	−0.109	16.7 ± 0.88
3.92	−0.282	17.0 ± 1.1
4.35	−0.422	18.6 ± 1.6
4.69	−0.535	20.0 ± 1.7
	$k = 5$ GeV	
0.847	0.788	139.7 ± 3.5
1.12	0.718	80.0 ± 3.2
1.35	0.662	53.4 ± 2.6
1.89	0.525	13.4 ± 1.2
2.37	0.405	8.14 ± 0.93
2.99	0.249	5.55 ± 0.70
3.85	0.034	3.46 ± 0.60
4.80	−0.206	2.17 ± 0.53
5.84	−0.467	3.07 ± 0.56
6.22	−0.562	3.34 ± 0.95
6.62	−0.662	6.24 ± 1.2

duction in the range of 25–50% of the production over the range of t values covered in this experiment. The combined cross sections ($\rho^0 + \omega$) shown in the figures and in Table VI are relatively insensitive to the assumed ratio of ω to ρ production. The forward t peak is known to be diffractive in nature, and so it leads to an e^{8t} dependence. At a $|t|$ of about 1(GeV/c)^2, the 4- and 6-GeV data break away from the characteristic diffraction peak, and show the general characteristics of the other exclusive channels. The 90° c.m. cross sections are about seven times the cross sections for the $\pi^+ n$ exclusive channel and about equal to the $\pi^- \Delta^{++}$ channel. The data of Ref. 14, 19, and 20 are also shown in Fig. 16.

IV. DISCUSSION

A. General features of the s and t dependence

Data at small t and u values have been provided by a number of experiments. These data have been represented by solid lines on Figs. 4, 7, 10, 13, and 16, where a comparison may be made at energies similar to the present experiment. Agreement between these diverse experiments is reasonably good. Phenomenologically, the data can be roughly

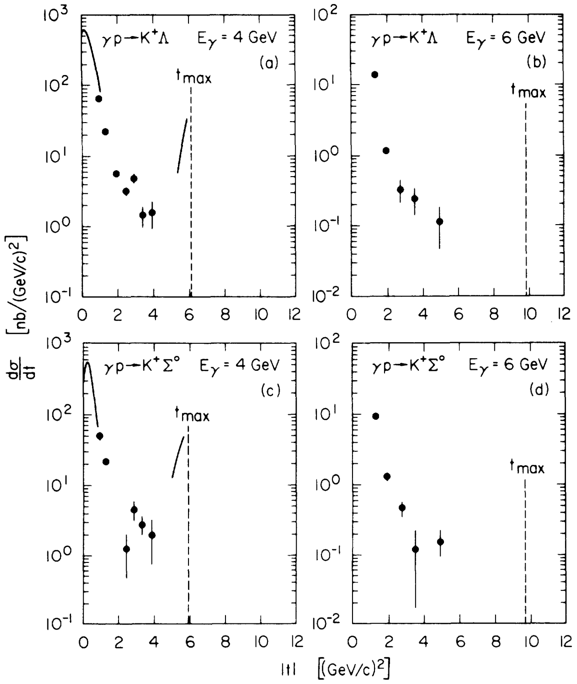

FIG. 13. $d\sigma/dt$ versus t for the reactions $\gamma p \to K^+\Lambda$ and $\gamma p \to K^+\Sigma^0$ at (a) and (c) $E_\gamma = 4.0$ GeV and (b) and (d) $E_\gamma = 6.0$ GeV.

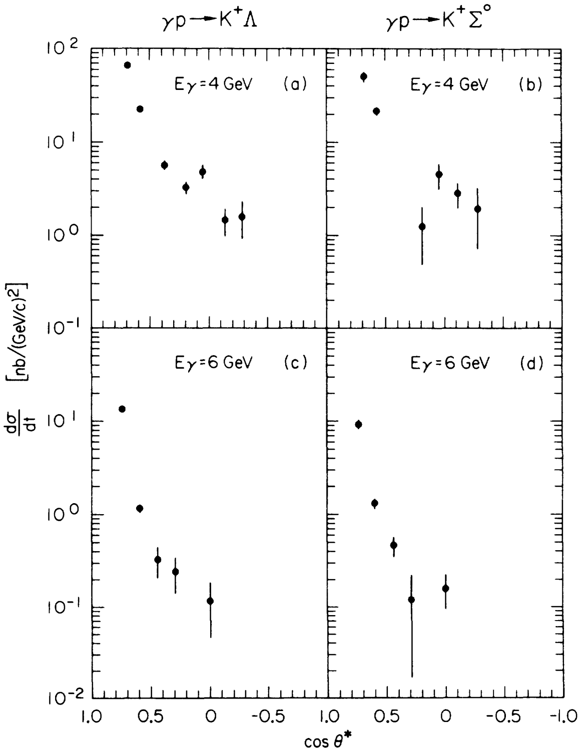

FIG. 14. $d\sigma/dt$ versus θ^* for the reactions $\gamma p \to K^+\Lambda$ and $\gamma p \to K^+\Sigma^0$ at (a) and (b) $E_\gamma = 4.0$ GeV and (c) and (d) $E_\gamma = 6.0$ GeV.

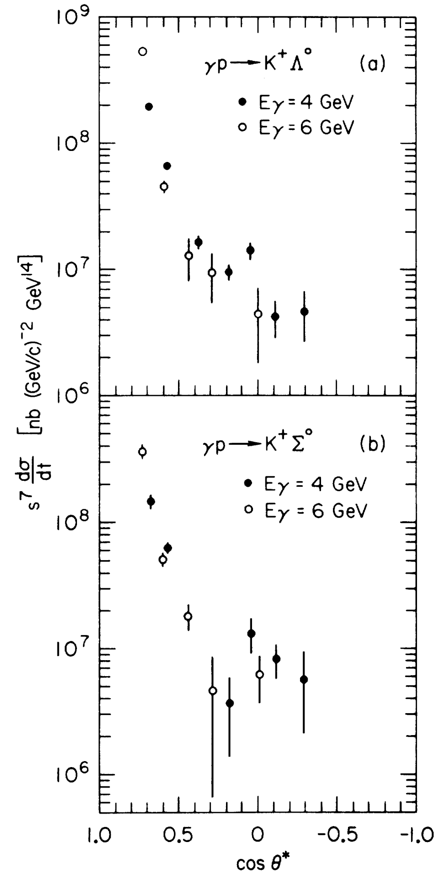

FIG. 15. $s^7\, d\sigma/dt$ versus $\cos\theta^*$ for the reaction (a) $\gamma p \to K^+\Lambda$ and (b) $\gamma p \to K^+\Sigma^0$.

TABLE V. Cross-section tabulation for the processes $\gamma p \to K^+\Lambda$ and $\gamma p \to K^+\Sigma^0$.

$-t$ [(GeV/c)^2]	$\cos\theta^*$	$d\sigma/dt$ [nb/(GeV/c)^2]
	$k = 4$ GeV $d\sigma/dt(\gamma p \to K^+\Lambda)$	
0.989	0.680	65.6 ±2.7
1.33	0.569	22.7 ±0.88
1.91	0.377	5.66 ±0.66
2.49	0.188	3.24 ±0.48
2.92	0.047	4.83 ±0.79
3.41	−0.114	1.44 ±0.47
3.92	−0.281	1.60 ±0.69
	$d\sigma/dt(\gamma p \to K^+\Sigma^0)$	
0.970	0.679	50.4 ±6.3
1.30	0.568	21.8 ±2.1
2.43	0.185	1.25 ±0.78
2.85	0.043	4.53 ±1.42
3.33	−0.118	2.81 ±0.84
3.82	−0.285	1.98 ±1.26
	$k = 6$ GeV $d\sigma/dt(\gamma p \to K^+\Lambda)$	
1.30	0.738	13.60 ±0.95
1.99	0.597	1.17 ±0.12
2.76	0.440	0.328 ±0.12
3.53	0.284	0.242 ±0.10
4.94	−0.003	0.115 ±0.069
	$d\sigma/dt(\gamma p \to K^+\Sigma^0)$	
1.29	0.736	9.3 ±1.1
1.97	0.595	1.31 ±0.17
2.72	0.439	0.46 ±0.12
3.48	0.282	0.12 ±0.10
4.86	−0.004	0.159 ±0.065

classified into a low t region extending out to $|t| \simeq 2.5$–3(GeV/c)^2 with an exponential t dependence, a central region with approximately a t-independent cross section, and a backward u-channel peak. For the case of vector-meson production, the forward t region can be split further into an energy-independent forward diffractive peak with an e^{8t} dependence followed by the three distinct regions discussed in Sec. III(E) above.

The three regions have properties which may be approximately summarized as follows

(1) The forward t region out to $|t| = 2.5$–3.0 (GeV/c)^2 has a t dependence of $\sim e^{3t}$ and an s^{-2} energy dependence at fixed t. There is little, if any, evidence for shrinkage of these forward peaks.

(2) The backward u-channel region from $u_{\min}$ out to $|u| \simeq 1.5$–2.0 (GeV/c)^2 has a flat u dependence of approximately $e^{1.5u}$ and an energy dependence at fixed u of approximately s^{-3}. There is no evidence for any shrinkage of these backward peaks.

(3) The remaining region, which is referred to as the central region in this paper, encompasses the remainder of the t distribution and has a steep energy dependence of $\sim s^{-7}$ at fixed c.m. angles. The angular distributions in this region range from an almost flat t dependence as observed in the 5-GeV $\pi^+ n$ data, to the t distributions observed in the $\pi^-\Delta^{++}$ and $(\rho^0+\omega^0)p$ data, where no distinct plateau is readily observed. Furthermore, a distinct structure is observed in the $\pi^0 p$ angular distributions, but the data are not extensive enough to determine if the structure has a fixed t behavior.

B. Specific features of the central region

1. Comparison of the 90° c.m. cross sections

The cross-section values are conveniently compared at 90° c.m. as a representative scattering angle of the central region. The 90° c.m. cross sections as a function of s are shown in Fig. 19. Interpolations of neighboring points have been made for the reactions which do not have a data point exactly at 90° c.m. The following features

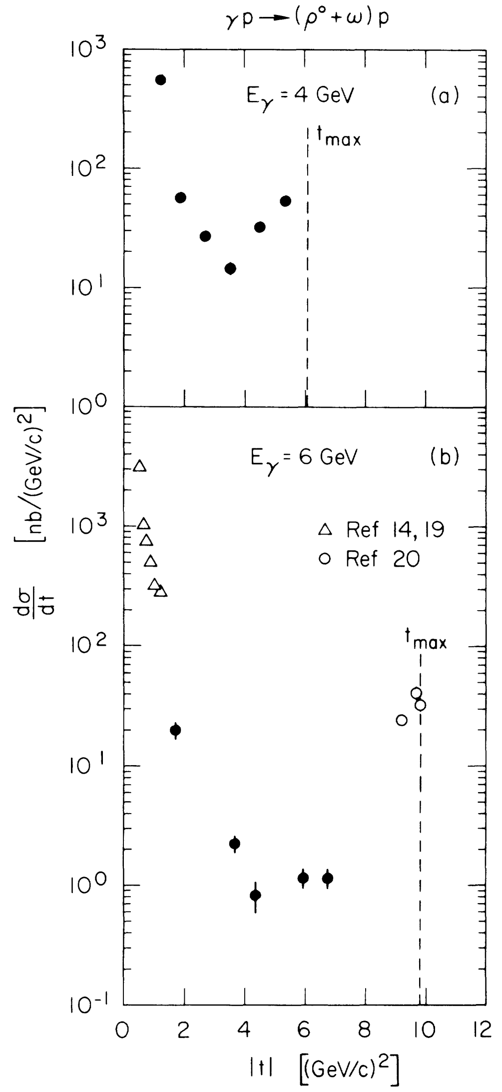

FIG. 16. $d\sigma/dt$ versus t for the reaction $\gamma p \to (\rho^0+\omega)p$ at (a) $E_\gamma = 4.0$ GeV and (b) $E_\gamma = 6.0$ GeV.

are apparent from this figure.

(a) The lowest cross sections at 90° c.m. are for the reactions $\gamma p \to \pi^+ n$ and $\gamma p \to K^+(\Lambda^0, \Sigma)$, which are approximately equal in value. The strange-particle cross sections are not as precise but the s dependence of both processes is consistent with s^{-7} (the s dependence for the three energies. specifically $s^{-7.3\pm.4}$), based on a simple fit to the 90° c.m. cross sections for the three energies.

(b) The $\gamma p \to \pi^0 p$ cross sections are approximately a factor of 2 larger than $\gamma p \to \pi^+ n$. The 90° c.m. s dependence is $s^{-7.6\pm0.7}$.

(c) The 90° c.m. cross sections for $\gamma p \to \pi^- \Delta^{++}$ and $\gamma p \to (\rho^0+\omega)p$ are substantially larger than $\gamma p \to \pi^+ n$ by approximately a factor of 6–7. The s depend-

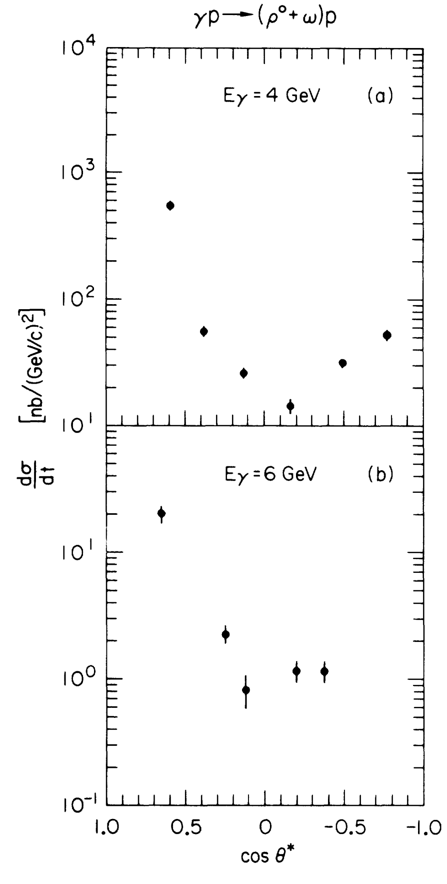

FIG. 17. $d\sigma/dt$ versus $\cos\theta^*$ for the reaction $\gamma p \to (\rho^0+\omega)p$ at (a) $E_\gamma = 4.0$ GeV and (b) $E_\gamma = 6.0$ GeV.

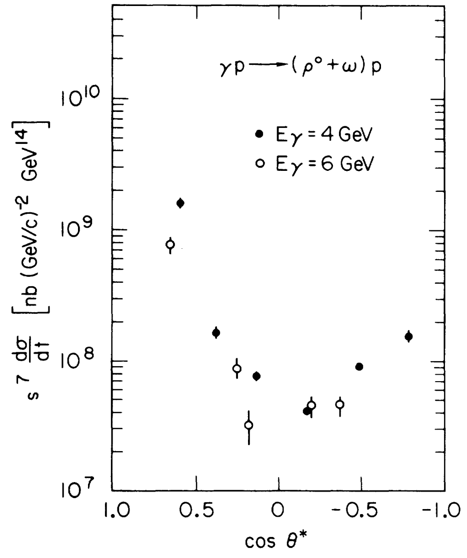

FIG. 18. $s^7 d\sigma/dt$ versus $\cos\theta^*$ for the reaction $\gamma p \to (\rho^0+\omega)p$.

TABLE VI. Cross-section tabulation for the process $\gamma p \to (\rho^0 + \omega)p$.

$-t$ [(GeV/c)^2]	$\cos\theta^*$	$d\sigma/dt$ [nb/(GeV/c)^2]
	$k = 4$ GeV	
1.25	0.589	555 ± 52
1.88	0.381	56.8 ± 5.7
2.66	0.125	26.5 ± 2.3
3.56	−0.172	14.5 ± 1.9
4.52	−0.489	31.4 ± 2.0
5.39	−0.777	53.3 ± 5.6
	$k = 6$ GeV	
1.75	0.644	20.0 ± 3.1
3.66	0.255	2.28 ± 0.39
4.33	0.118	0.83 ± 0.25
5.89	−0.200	1.16 ± 0.22
6.75	−0.375	1.17 ± 0.21

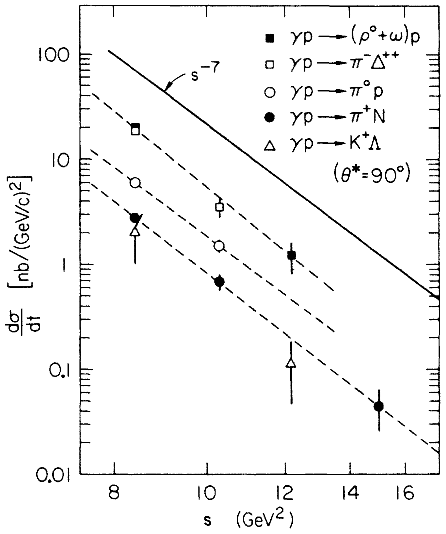

FIG. 19. 90° c.m. values of $d\sigma/dt$ versus s for some of the processes measured in this experiment. The function s^{-7} is shown as a solid line for reference, and the dashed lines represent the trend of the data.

ence of $\gamma p \to \pi^- \Delta^{++}$ is $s^{-8.6 \pm 0.8}$. The $\gamma p \to (\rho^0 + \omega)p$ statistics are not good enough to make a meaningful s-dependence comparison, but the s dependence is consistent with that of the other processes. It is interesting to note that these two processes with the highest 90° c.m. cross sections involve final-state particles with higher spin, viz. the ρ^0, ω, and Δ^{++}.

2. The scaling features of the cross sections

The data of this experiment are primarily concentrated in the region $-0.6 \leq \cos\theta^* \leq 0.6$, and the figures showing $s^7 d\sigma/dt$ versus $\cos\theta^*$ indicate that an s^{-7} energy dependence at a fixed angle is a fairly good representation of the cross sections. The angular distributions are also qualitatively similar for all reactions, but no detailed functional comparison has been made. These aforementioned properties indicate that the data can be represented approximately by $d\sigma/dt \sim s^{-7} f(\cos\theta^*)$, showing qualitatively that the s and $\cos\theta^*$ dependences show a simple scaling behavior.

3. Extrapolation to the resonance region

It is of interest to examine the central-region cross sections with an s^{-7} extrapolation back to the resonance region (~700 − 1000 MeV). This extrapolation is shown in Fig. 20 for the reaction $\gamma p \to \pi^+ n$, and shows the data of the present experiment, together with lower energy 90° c.m. data from MIT[21] and Caltech.[22] Again, this sort of comparison is qualitative in nature, but an s^{-7} extrapolation from the 4–7.5 GeV region is in fairly good agreement with 90° c.m. cross sections down to ~700 MeV photon energy, where resonance phenomena have become increasingly important. This suggests that the central region is correlated with s-channel processes and is perhaps related closely to low-energy photon processes.

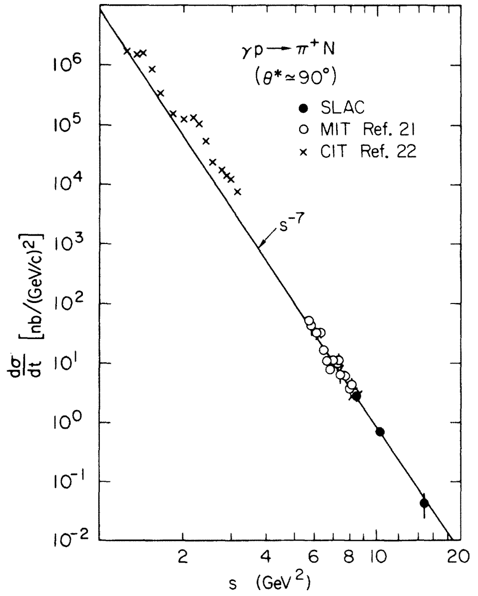

FIG. 20. 90° c.m. values of $d\sigma/dt$ versus s for the process $\gamma p \to \pi^+ n$ from several experiments from $E_\gamma = 700$ MeV to $E_\gamma = 7.5$ GeV. The solid line shows the function s^{-7} for reference.

C. Comparison of the photoproduction reactions with pion-nucleon scattering

Figure 21 shows a comparison of 5-GeV $\gamma p \rightarrow \pi^+ n$ data multiplied by a scale factor, and the corresponding $\pi^+ p$ and $\pi^- p$ elastic scattering[23] and $\pi^- p$ charge-exchange data.[24] The πp data show the same qualitative features of forward and backward peaks and a central region dropping with a large s dependence. As can be seen from Fig. 21, the backward peak and central region can be approximately represented by the form:

$$d\sigma/dt(\gamma p \rightarrow \pi^+ n) \simeq \tfrac{1}{2}[d\sigma/dt(\pi^+ p \rightarrow \pi^+ p) + d\sigma/dt(\pi^- p \rightarrow \pi^- p)]\tfrac{1}{217}. \tag{1}$$

The factor 217 is the ratio of the γp total cross section[25] to the average of the $\pi^+ p$ and $\pi^- p$ total cross sections.[26] This factor scales the $\gamma p \rightarrow \pi^+ n$ and πp elastic differential cross sections very well, thus showing the close correspondence between large-angle photoproduction and hadronic processes. The marked dips of the pion data seem to be absent in the photoproduction $\gamma p \rightarrow \pi^+ n$ data. The s dependence observed for the 90° c.m. pion data is also very close to that observed in the photoproduction data and is qualitatively consistent with s^{-8} behavior.

A strict application of vector-dominance and quark-model relations leads to a similar relation with somewhat different numerical values. Explicitly, in terms of the photon-ρ meson coupling constant, the relation is

$$\frac{d\sigma}{dt}(\gamma p \rightarrow \pi^0 p) = \frac{\alpha}{4}\left(\frac{\gamma_\rho^2}{4\pi}\right)^{-1}\frac{1}{2}\left[\frac{d\sigma}{dt}(\pi^+ p \rightarrow \pi^+ p) + \frac{d\sigma}{dt}(\pi^- p \rightarrow \pi^- p)\right]. \tag{2}$$

The numerical factor $\frac{1}{217}$ in Eq. (1), deduced from the ratio of total cross sections, now becomes $(\alpha/4)(\gamma_\rho^2/4\pi)^{-1} = \frac{1}{350}$.[27] Since the $\gamma p \rightarrow \pi^0 p$ cross sections are approximately a factor of 2 larger than the $\gamma p \rightarrow \pi^+ n$ values, the above relation (Eq. 2) underestimates the $\gamma p \rightarrow \pi^0 p$ cross section by approximately a factor of 3.

D. Features of large angle photoproduction of strange particles

The cross sections for the processes $\gamma p \rightarrow K^+ \Lambda$ and $\gamma p \rightarrow K^+ \Sigma^0$ have larger statistical errors than most of the other cross sections measured in this experiment, but some general features are readily apparent.

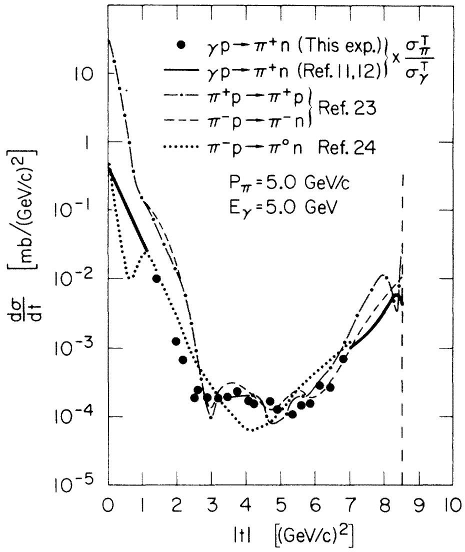

FIG. 21. Comparison of $E_\gamma = 5.0$ GeV $\gamma p \rightarrow \pi^+ n$ data of this experiment with $\pi^\pm p \rightarrow \pi^\pm p$ elastic scattering and $\pi^- p$ charge exchange at $p_\pi = 5.0$ GeV/c. The photoproduction cross sections have been scaled by the total-cross-section ratio $\sigma_\pi^T/\sigma_\gamma^T$.

(1) As determined from data at 4 GeV and 6 GeV, the central-region s dependence is consistent with an s^{-7} behavior at fixed angle. The data are not precise enough for a meaningful quantitative determination of the s dependence power. The angular distributions are also similar to those of the other photoproduction processes.

(2) The central-region cross sections are approximately the same magnitude as for $\gamma p \rightarrow \pi^+ n$, but clearly lower than $\gamma p \rightarrow \pi^0 p$ and the remaining processes. There is no obvious suppression of central-region strange-particle exclusive photoproduction.

(3) The central-region Λ/Σ^0 ratio is consistent with unity. The Λ/Σ^0 ratio plotted as a function of t is shown in Fig. 22.

E. Features of constituent scattering models and comparison with experiment

1. Constituent scattering models

A class of models dealing with large-transverse-momentum collisions is based on the point-like behavior that has been observed in inelastic electron scattering. These models are based on the notion that hadrons can scatter at large angles (or large $p_\perp$) through hard collisions between their constituents. For example, pion photoproduction may be considered as pion photoproduction from one of the nucleon constituents, viz:

$$\frac{d\sigma}{dt}(\gamma n \rightarrow \pi n) \cong F_N{}^2(t)\frac{d\sigma}{dt}(\gamma q \rightarrow \pi q), \tag{3}$$

where $F_N(t)$ is the nucleon form factor and $\gamma q \rightarrow \pi q$ is the pion production from constituent q. In general, constituent models for exclusive scattering processes predict the following general form for the cross section:[2]

$$\frac{d\sigma}{dt}(s,t) \sim \frac{1}{s^N} F\left(\frac{t}{s}\right). \tag{4}$$

Such a dependence implies a power-law s dependence at fixed c.m. scattering angle.

The power-law behavior of the s dependence is given by some general dimensional-counting rules based on the number of elementary constituents involved in the large-angle scattering process. In general, for the reaction $A+B \rightarrow C+D$, the exponent N is given by[6,7]

$$N=(m_A+m_B+m_C+m_D-2), \tag{5}$$

where $m_A \cdots m_D$ are the number of elementary constituents in particles $A \cdots D$, respectively. Then, specifically, for photoproduction, if the photon is considered to be a single elementary constituent, the meson-photoproduction cross section would be expected to go as

$$\frac{d\sigma}{dt} \sim \frac{1}{s^7} f(\cos\theta^*), \tag{6}$$

while proton-proton scattering would have an s^{-10} behavior.

A specific model is the constituent-interchange model of Brodsky, Blankenbecler, and Gunion,[3] which is based on the dominance of constituent interchange (as opposed, for example, to constituent-constituent scattering). Some specific predictions based on this model may be found in the paper by Gunion.[28] Recently, Scott applied the parton model to inclusive and exclusive photoproduction processes[29] and this reference should be consulted for detailed predictions of the exclusive-process angular distributions.

The parton ideas have also been used extensively to describe inclusive phenomena at large transverse momenta, and the correspondence principle of Bjorken and Kogut provides a connection between inclusive and exclusive processes. This principle relates the integral over the resonance region of particle inclusive cross sections to exclusive cross sections for producing the particle or resonance via the relation

$$\int_R E\,\frac{d^3\sigma}{d^3p}\,dE \sim \sum_R \frac{1}{E}\,\frac{d\sigma}{d\Omega}, \tag{7}$$

where R indicates a sum or integral over the resonance region.[8] A companion experiment to the present set of exclusive measurements is currently being analyzed, and the connection between exclusive and inclusive processes will be discussed in a subsequent paper.

2. Comparison with experiment

The most general feature of the constituent models is the fixed-angle s dependence predicted to be $\sim s^{-7}$ by the dimensional-counting arguments and the constituent-interchange model. Figures 6, 9, 12, 15, and 18 show the cross sections plotted as a function of $\cos\theta^*$ with an s^7 factor taken out. All the processes studied in this experiment are consistent with an s^{-7} power behavior over essentially the full range of c.m. angles, and therefore this scaling form gives a good representation of the data. The precision of the determination of the power exponent, however, is no better than half a unit for the process $\gamma p \rightarrow \pi^+ n$ and less precise for all the other processes. The exponent

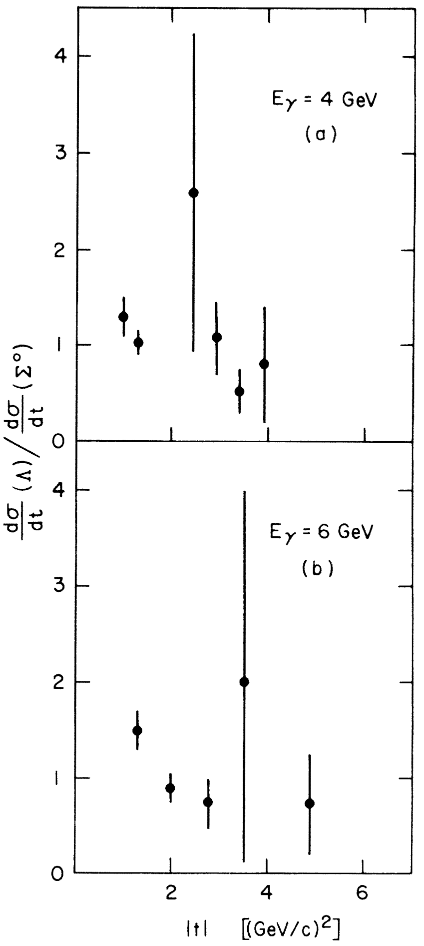

FIG. 22. The ratio of the cross sections $d\sigma/dt$ for the processes $\gamma p \rightarrow K^+\Lambda$ and $\gamma p \rightarrow K^+\Sigma^0$ versus t at (a) $E_\gamma = 4.0$ GeV and (b) $E_\gamma = 6.0$ GeV.

m for s^{-m} at 90° c.m. for the various processes is given in Sec. IV(B), and the 90° c.m. cross sections for each process are plotted in Fig. 19.

The angular distributions in the central region show a rapid variation with angle, as can be seen in Figs. 5, 8, 11, 14, and 17, and they are qualitatively similar for all the reactions. A solid line in Fig. 6 for the $\gamma p \rightarrow \pi^+ n$ reaction shows the empirical function $(1-z)^{-5}(1+z)^{-4}$, where $z = \cos\theta^*$. This angular distribution function qualitatively fits the data. No attempt has been made to make a polynomial fit to these data since fairly high powers of z are involved if the whole angular distribution were to be fit, and since the general region of validity for the constituent models is only approximately known. The detailed predictions given in Ref. 28 and 29 for the angular distributions do not agree well with the data. These predictions tend to show considerably more skewing about 90° c.m. than is actually observed.

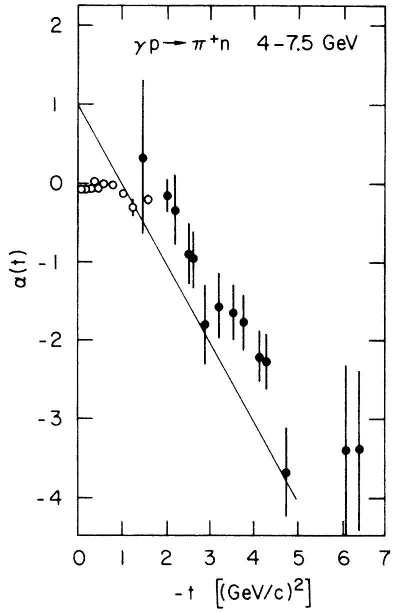

FIG. 23. The Regge parameter $\alpha(t)$ as a function of t for the process $\gamma p \rightarrow \pi^+ n$ as determined by cross-section data from $E_\gamma = 4.0$ to $E_\gamma = 7.5$ GeV. The function $\alpha(t) = 1 + t$ is indicated by a solid line and is shown for comparison purposes only.

F. The energy dependence in terms of a Regge parametrization

It is instructive to look at the energy dependence of these processes in terms of Regge parameters. From an examination of $\alpha(t)$ as a function of t, it should be readily apparent where the departure from the forward-peak s^{-2} fixed-t behavior to the steeper s dependence in the central region takes place. This parametrization has been made for the reaction $\gamma p \rightarrow \pi^+ n$. Figure 23 shows $\alpha(t)$ as a function of t for the reaction $\gamma p \rightarrow \pi^+ n$ for the data of this experiment and the data of Ref. 11.

As can be seen from this figure, the parameter $\alpha(t)$ (defined by $d\sigma/dt \sim s^{2[\alpha(t)-1]}$) is nominally zero or slowly decreasing out to $-t \simeq 2$ (GeV/c)^2 and then breaks away to a steep energy dependence with approximately a unit slope. $\alpha(t) = 1 + t$ is shown in the figure by a solid line simply for comparison purposes.

G. The process $\gamma p \rightarrow (\rho^0 + \omega)p$ and the relation to compton scattering

A fundamental process from the standpoint of constituent-scattering models is large-angle Compton scattering. Constituent-scattering models of the above types will apply to this process, and similar predictions can be made. However, this process can be treated more specifically since $\gamma p \rightarrow \gamma p$ in a constituent-scattering model is simply the elastic scattering of photons from the constituents; an absolute-cross-section expression for scattering from spin-$\frac{1}{2}$ constituents in terms of constituent charges, the proton form factor, and the Klein-Nishina cross section would be

$$\frac{d\sigma}{dt}(\gamma p \rightarrow \gamma p) = \frac{d\sigma}{dt}(\text{Klein-Nishina})\langle Q^2\rangle^2 G_E{}^2(t)\,, \quad (8)$$

where $\langle Q^2\rangle$ is the square of the effective constituent charges and

$$G_E(t) = \frac{1}{(1 - t/0.71)^2} \quad (9)$$

is the proton form factor.

In terms of s, t, and u variables, this expression becomes:

$$\frac{d\sigma}{dt}(\gamma p \rightarrow \gamma p) = \frac{2\pi\alpha^2}{(s-M^2)^2}\left[\left(\frac{s+M^2}{s-M^2} - \frac{2M^2}{s+t-M^2}\right)^2 + \frac{t}{s-M^2} + \frac{s-M^2}{s+t-M^2}\right]\langle Q^2\rangle^2 G_E{}^2(t) \simeq \frac{2\pi\alpha^2}{s^2}\,\frac{4}{9}\left(\frac{s^2+u^2}{-su}\right) G_E{}^2(t)\,, \quad (10)$$

using $\langle Q^2\rangle = \frac{2}{3}$, and neglecting the nucleon mass M. A more detailed discussion of parton-model calculations for Compton scattering may be found in the papers of Bjorken and Paschos[30] and Scott.[31]

While large-angle exclusive Compton scattering has not been measured in this experiment, the exclusive large-angle photoproduction of ρ mesons (or $\rho^0 + \omega$) has been measured, and can be used to set a lower limit on the Compton-scattering cross section through the use of the vector-dominance relation:

$$\frac{d\sigma}{dt}(\gamma p\to\gamma p)_{\rm VD}=\frac{\alpha}{4}(\gamma_\rho{}^2/4\pi)^{-1}\,d\sigma/dt(\gamma p\to\rho^0 p)_{\rm tr}\,. \quad (11)$$

Using the storage ring value of $\gamma_\rho{}^2/4\pi=0.64\pm.05$ gives

$$\frac{d\sigma}{dt}(\gamma p\to\gamma p)_{\rm VD}=\frac{1}{350}\frac{d\sigma}{dt}(\gamma p\to\rho^0 p)_{\rm tr}\,. \quad (12)$$

Taking $\frac{1}{2}$ the measured cross section for $d\sigma/dt$ $(\gamma p\to(\rho^0+\omega)p)$ as a representative cross section for $(\gamma p\to\rho^0 p)_{\rm tr}$ yields

$$4\ {\rm GeV}(90^\circ\ {\rm c.m.}):\ \frac{d\sigma}{dt}(\gamma p\to\gamma p)_{\rm VD}\cong 3\times10^{-2}\,\frac{\rm nb}{({\rm GeV}/c)^2}$$

and

$$6\ {\rm GeV}(90^\circ\ {\rm c.m.}):\ \frac{d\sigma}{dt}(\gamma p\to\gamma p)_{\rm VD}\cong 1.5\times10^{-3}\,\frac{\rm nb}{({\rm GeV}/c)^2}$$

based on the data of Table 6.

These cross-section values are to be compared with the estimates based on Eq. (10), but nucleon mass terms are kept. The resulting constituent-model cross sections are

$$4\ {\rm GeV}\,\frac{d\sigma}{dt}(\gamma p\to\gamma p)_{90^\circ{\rm c.m.}}=0.19\times10^{-2}\,\frac{\rm nb}{({\rm GeV}/c)^2}$$

and

$$6\ {\rm GeV}\,\frac{d\sigma}{dt}(\gamma p\to\gamma p)_{90^\circ{\rm c.m.}}=0.20\times10^{-3}\,\frac{\rm nb}{({\rm GeV}/c)^2},$$

indicating substantially higher cross sections arising from Compton scattering through vector dominance than those deduced from the elementary constituent scattering.

V. CONCLUSIONS

These data present a comprehensive picture of the exclusive photoproduction processes in the 4- to 6-GeV region. The results are in reasonable agreement with previous forward- and backward-angle measurements for meson photoproduction. In addition, there is a large t and u central region with distinct properties. The s dependence of the cross sections in the central region is similar to that observed for pion-proton scattering and close to that predicted by constituent-scattering models and dimensional-counting rules. In particular, these models predict an s^{-7} behavior for $\gamma p\to\pi^+ n$ reactions at a fixed angle in good agreement with the data. In the forward direction, the transition to the central region appears to start at $|t|\sim 2$ $({\rm GeV}/c)^2$ where the s dependence of s^{-2} gradually changes to the s^{-7} behavior observed near 90° c.m.

The central-region cross sections for all channels, including the exclusive photoproduction of kaons and ρ's are similar, but the $\pi^-\Delta^{++}$ and $(\rho^0+\omega)p$ cross sections are approximately a factor 6–7 larger. The angular distribution for all channels are also similar with an approximate $(1-z)^{-5}$ $(1+z)^{-4}$ behavior. However, the $\pi^-\Delta^{++}$ and $(\rho^0+\omega)p$ cross sections appear to be more skewed about 90° c.m. with the cross-section minima being closer to $\cos\theta^*\simeq-0.2$. Some conclusions for specific channels are as follows:

(1) The processes $\gamma p\to\pi^+ n$ and $\gamma p\to\pi^0 p$ show similar qualitative features of forward and backward peaks separated by a central region falling with a steep s dependence. The central-region cross sections are approximately symmetric about 90° c.m. The s dependence at 90° c.m. is characterized by s^{-m} with $m=7.3\pm0.4$ for $\pi^+ n$ and $m=7.6\pm0.7$ for $\pi^0 p$.

(2) There is evidence for t structure in the 4-GeV π^0 data at $|t|=2.5$ and 4.5 $({\rm GeV}/c)^2$. The πp elastic-scattering channels at 5 GeV show considerable structure in these t regions.

(3) The central-region cross sections for the $\pi^-\Delta^{++}$ and $(\rho^0+\omega)p$ channels are significantly higher than the $\pi^+ n$ and $\pi^0 p$ values at 4 and 5 GeV, while the forward-peak cross sections are all approximately the same in the region $0.2\leqslant|t|\leqslant1.2$ $({\rm GeV}/c)^2$, except for the π^0 dip at $t\cong-0.5({\rm GeV}/c)^2$. The minima for the $\pi^-\Delta^{++}$ and $(\rho^0+\omega)p$ cross sections occur at a somewhat greater value than 90° c.m.

(4) The production of strange particles via $\gamma p\to K^+\Lambda$ and $\gamma p\to K^+\Sigma^0$ is similar to the production of nonstrange mesons with central-region cross sections similar in magnitude to $\gamma p\to\pi^+ n$. The s dependence is consistent with an s^{-7} fixed-angle behavior. The Σ^0/Λ ratio is consistent with unity in the central region, as is also the case in the forward t-channel peaks.

(5) $\rho+\omega$ exclusive photoproduction has a forward diffractive peak with an e^{8t} t dependence showing a slight s dependence, a region with an e^{3t} and s^{-2} dependence that is important in the t region of 1–3 $({\rm GeV}/c)^2$, a central region qualitatively similar to the other processes, and a backward u-channel peak.

ACKNOWLEDGMENTS

We would like to thank B. Gottschalk for his work on the early phases of the experiment, and M. S. Witherell for assistance with the data-taking. We would like to express our appreciation to the Spectrometer Facilities Group for their support, and finally we would like to thank J. Escalera, J. Schroeder, and J. Grant for their invaluable assistance.

*Work supported by the U. S. Energy and Research Development Administration.

†Present address: CEN Saclay, BP2, 91190, Gif-sur-Yvette, France.

‡Present address: Carnegie-Mellon University, Pittsburgh, Pennsylvania 15213.

§Present address: U. S. Geological Survey, Menlo Park, California 94025.

[1] R. L. Anderson *et al.*, Phys. Rev. Lett. 30, 627 (1973).

[2] D. Sivers, S. J. Brodsky, and R. Blankenbecler, 23C, 1 (1976).

[3] J. F. Gunion, S. J. Brodsky, and R. Blankenbecler, Phys. Rev. D 8, 287 (1973).

[4] P. V. Landshoff and J. C. Polkinghorne, Phys. Rev. D 8, 927 (1973).

[5] J. F. Gunion, S. J. Brodsky, and R. Blankenbecler, Phys. Lett. 39B, 649 (1972).

[6] V. A. Matveev, R. M. Muradyan, and A. N. Tavkhelidze, Lett. Nuovo Cimento 7, 719 (1973).

[7] S. J. Brodsky and G. Farrar, Phys. Rev. Lett. 31, 1153 (1973).

[8] J. D. Bjorken and J. Kogut, Phys. Rev. D 8, 1341 (1973).

[9] R. L. Anderson, Nucl. Instrum. Methods 65, 195 (1968); G. E. Fischer and Y. Murata, *ibid.* 78, 25 (1970).

[10] SLAC Users Handbook (revised edition, March, 1973).

[11] A. M. Boyarski *et al.*, Phys. Rev. Lett. 20, 300 (1968).

[12] R. L. Anderson *et al.*, Phys. Rev. Lett. 23, 721 (1969).

[13] M. Braunschweig *et al.*, Phys. Lett. 26B, 405 (1968).

[14] R. L. Anderson *et al.*, Phys. Rev. D 1, 27 (1970).

[15] A. M. Boyarski *et al.*, Phys. Rev. Lett. 22, 148 (1969).

[16] R. L. Anderson *et al.*, Phys. Rev. Lett. 23, 721 (1969).

[17] A. M. Boyarski *et al.*, Phys. Rev. Lett. 22, 1131 (1969).

[18] R. L. Anderson *et al.*, Phys. Rev. Lett. 23, 890 (1969).

[19] B. Barish *et al.*, Phys. Rev. D 9, 566 (1974).

[20] D. H. Tompkins *et al.*, Phys. Rev. Lett. 23, 725 (1969).

[21] R. Alvarez *et al.*, Phys. Rev. Lett. 12, 707 (1964).

[22] R. L. Walker, Phys. Rev. 182, 1729 (1969).

[23] V. Chaubaud *et al.*, Phys. Lett. 38B, 441 (1972).

[24] W. S. Brocket *et al.*, Phys. Rev. Lett. 26, 527 (1971).

[25] H. Meyer *et al.*, Phys. Lett. B33, 189 (1970); D. O. Caldwell *et al.*, Phys. Rev. Lett. 25, 609 (1970), *ibid.* 25, 902 (1970).

[26] A. Citron *et al.*, Phys. Rev. 144, 1101 (1966).

[27] D. Benaksas *et al.*, Phys. Lett. 39B, 289 (1972).

[28] J. F. Gunion, in *Particles and Fields—1974,* proceedings of the 1974 Williamsburg meeting of the Division of Particles and Fields of the American Physical Society, edited by Carl E. Carlson (A. I. P., New York, 1975) p. 551.

[29] D. M. Scott, Phys. Lett. 59B, 171 (1975).

[30] J. D. Bjorken and E. A. Paschos, Phys. Rev. 185, 1975 (1969).

[31] D. M. Scott, Phys. Rev. D 10, 3117 (1974).